Construction and Building Materials 319 (2022) 126098

Contents lists available at ScienceDirect

Construction and Building Materials

journal homepage: www.elsevier.com/locate/conbuildmat

Radiation shielding properties of siderurgical aggregate concrete

P. Tamayo [a], C. Thomas [a,*], J. Rico [b], S. Pérez [b], A. Mañanes [c]

[a] LADICIM (Laboratory of Materials Science and Engineering), University of Cantabria, E.T.S. de Ingenieros de Caminos, Canales y Puertos, Av./Los Castros 44, 39005 Santander, Spain
[b] Construction Engineering, Research and Project Development (INGECID S.L.), E.T.S. de Ingenieros de Caminos, Canales y Puertos, Av./Los Castros 44, 39005 Santander, Spain
[c] Department of Modern Physics, University of Cantabria, Faculty of Sciences, Av./Los Castros 48, 39005 Santander, Spain

ARTICLE INFO

Keywords:
Radiation shielding
Concrete
EAFS
Siderurgical aggregates
Magnetite
Neutron
Gamma
w/c ratio
Cement

ABSTRACT

The world is changing, and consequently so are policies on the use of natural resources. One of the most convenient ways to reduce the consumption of natural aggregates in the production of more sustainable construction materials is the use of recovered industrial by-products. In this study, concretes are designed using siderurgical aggregates from electric arc furnaces, taking advantage of their high density to use them as radiation shielding concrete. To verify the suitability of these aggregates, four concrete mixes were designed with different aggregates: limestone, siderurgical magnetite aggregates (the most commonly used in the nuclear field). The comparison of the different mixes was carried out focusing on the physical–mechanical properties in the field of ionizing radiation shielding (gamma radiation and neutron shielding) by means of simulations. In addition, an analysis was performed to establish how the w/c ratio and the amount of CEM affect shielding properties. In terms of linear attenuation coefficient and neutron transmission rate, the concrete with siderurgical aggregates shows intermediate capability in comparison with the limestone aggregate and magnetite concrete. The increase in the amount of cement and the w/c ratio caused a decrease in the linear attenuation coefficient and a reduction in the neutron transmission rate, but the variation in the w/c ratio did not have a significant impact on the neutron transmission rate.

1. Introduction

The search for new materials and the optimization of the design of shielding structures are two main objectives in the science and technology of nuclear shielding materials. The most commonly used material for this purpose is concrete [1] due to its low cost, ease of installation, mechanical properties and ability to attenuate both gamma and neutron radiation [2]. On the other hand, current policies, for example within the framework of the European Union [3], are focused on using more sustainable construction materials that are associated with lower CO_2 emissions. In the case of siderurgical aggregates (SA) this reduction can reach 35% [4]. From the combination of these two concepts arises the idea of designing concrete with SA in order to obtain eco-concrete with effective radiation shielding.

The two main types of ionizing radiation are gamma radiation and neutron radiation. The attenuation of gamma rays (photons) through a material occurs exponentially with the thickness of the absorber. This attenuation follows Lambert's Law [5] and is highly dependent on the density of the shielding material. In general, it can be considered that a 25% increase in density gives concrete an increase in the attenuation coefficient (μ) of around 10% [6]. High-density concretes use aggregates with densities greater than 3000 kg/m^3 [7], which are mainly composed of iron oxides such as goethite, barite or magnetite [8,9], providing a density of 4000 kg/m^3 [10]. Other materials of a metallic ferrous nature such as iron balls and punchings have been used successfully in the literature to increase the density of concrete [5,11].

The attenuation of fast neutrons can be estimated with the Albert–Welton Kernel expression [12] and the effective cross-section Σ_R ($\Sigma_R = \Sigma_{scattering} + \Sigma_{absorption}$). Σ_R is the probability that a fast neutron undergoes an interaction that removes it from the penetrating radiation group [13]. The necessary conditions are that there is sufficient moderating material and energies of 2–12 MeV [14]. Concrete is composed of light nuclei (large $\Sigma_{scattering}$) that increase the probability of an elastic scattering type interaction, thermalizing fast neutrons [14]. The two natural elements with the highest neutron scattering cross section are H and C (an order of magnitude less than the former), so

* Corresponding author.
E-mail address: carlos.thomas@unican.es (C. Thomas).

https://doi.org/10.1016/j.conbuildmat.2021.126098
Received 14 September 2021; Received in revised form 25 November 2021; Accepted 12 December 2021
Available online 17 December 2021

large amounts of cement (CEM) will provide a greater amount of C-based and hydrated products. Aggregates with a high C content such as carbonates (limestone, dolomite or marl) can also be used, as can polymeric nature materials such as polypropylene [15] or polyvinyl alcohol [16] fibers included in concrete. Once thermalized, materials with large absorption cross section ($\Sigma_{absorption}$) are responsible for capturing the thermal neutrons by radiative capture. In shielding concrete, natural aggregates with great $\Sigma_{absorption}$ (boron based) such as colemanite [17], ferroboron [18] or borocalcite [19] can be used with the great disadvantage that they show CEM hydration retarding character [20]. Boron-based fillers such as boron carbide [21] or boron nitride [22] can also be used for this purpose.

Moreover, there are studies in the literature using computing sequences such as Monte Carlo N-Particle Transport (MCNP) [23,24] or MAVRIC [25] that enable the interactions of materials with radiation to be modeled, facilitating the tracking of all particles and energies. These simulations enable experimental results to be collated and, once validated, complex models to be developed. MAVRIC can perform deep penetration radiation simulations with automatic variance reduction using adjoint-biased source and importance mapping to improve the Monte Carlo computational speed [26]. The simulations performed are often used to analyze critical variables in radiation shielding, after validation with the experimental model.

There are new uses for SA in concrete, specifically after valuing electric arc furnace slags (EAFS), such as the production of recycled concrete [27] or high performance self-compacting concrete [28] but the use of SA in concrete for radiological purposes is something new and a potential application that needs to be explored. Recently, some authors checked the response to gamma radiation using a ^{137}Cs source [29,30], but more sources and neutron responses have to be characterized. On the other hand, the environmental and economic feasibility of SA in concrete has been widely demonstrated [31–35]. There again, although there are numerous studies that demonstrate the influence of the w/c ratio on the fracture and mechanical characteristics of concretes [36], there are hardly any research works that analyze the effect on shielding properties. Kharita et al. [37] analyzed, in limestone concrete, the influence of the initial w/c ratio on the linear attenuation coefficient of ^{137}Cs and on the neutron attenuation of an Am-Be source without finding great effects. Şahin et al. [38] analyzed how the w/c ratio, the amount of CEM and the air entraining agent affect the transmission of gamma radiation for energies between 30.85 and 383.85 keV, being lower with lower w/c ratios. Yadollahi et al., [39] applied artificial neural networks to predict the response of thermal neutron shielding by varying the w/c ratio and the quantity of CEM with a source of ^{252}Cf, obtaining the optimum values for w/c ratios and quantity of CEM of 0.38 and 400 kg/m^3 respectively.

The simulations carried out in this study were performed with an experimental validation, using a wide range of gamma source energy with isotopes of ^{137}Cs, ^{60}Co, ^{22}Na and ^{207}Bi and a neutron source of Am-Be. In this research, the MAVRIC computational sequence in the SCALE 6.2.3 code package was used to analyze models that include five w/c ratios (0.39, 0.43, 0.47, 0.51 and 0.55) and five amounts of CEM (260, 300, 340, 380 and 420 kg/m^3) for mixes that incorporate four different aggregate combinations (limestone, limestone-SA, SA and magnetite) with identical proportions under the assumption that they operate at high temperatures (there is no unbound water). The main physical–mechanical properties of the four main mix proportions (w/c = 0.47 and amount of CEM = 340 kg/m^3) were been obtained to establish the comparison of the aggregates used in the physical–mechanical dimension.

The simulations made it possible to establish two main conclusions. The first was to demonstrate the feasibility of using SA by comparing it with a conventional concrete (limestone) and a concrete specialized in radiation shielding (magnetite). The second was to establish how both the w/c ratio and the amount of CEM affect the shielding properties of the concrete, considering the existing dichotomy when increasing the amount of CEM (decrease in μ and increase in Σ_R) and the effect of increasing the w/c ratio (decrease in μ and maintenance of Σ_R but decrease in workability).

2. Methodology

2.1. Materials and mix proportions

Limestone aggregates of size 12–18 mm (LC1), 6–12 mm (LC2) and 0–6 mm (LS1) were used. The siderurgical aggregates used are sizes 8–16 mm (SC1), 4–8 mm (SC2), 0–4 mm (SS1) and 0–2 mm (SS2). Finally, the magnetite aggregates used include the fractions 0–20 mm (MC1) and 0–8 mm (MS1). Within the physical properties of aggregates, the apparent specific density, bulk specific density and saturated surface dry (SSD) density were determined following EN 1097–3 [40] and the water absorption and porosity were determined following EN 1097–6 [41]. Table 1 shows the properties of the aggregates used. Note that magnetite aggregate is 80% denser than limestone and 20% denser than siderurgical aggregate. On the other hand, the water absorption values were lower than the 5% limit of EHE-08 [42] and the Spanish Structural Code [43] for structural concrete.

The research is based on the comparison of a SA concrete with conventional concrete and also on the comparison with the most commonly used aggregate for shielding purposes (magnetite concrete) to verify the goodness of siderurgical aggregates.

The four mixes (Table 2) were designed by the Fuller method using the same amount of water, CEM (CEM I 52.5R [44]), superplasticizer additive and the same volume of aggregates, to facilitate comparison:

- A reference limestone concrete mix with fines and coarse limestone fractions (LLC).
- A concrete mix with fine and coarse siderurgical aggregate fractions, which also incorporated limestone sand (SLC) to compensate for the lack of fines.
- A concrete mix with fine and coarse siderurgical aggregate fractions, which also incorporated crushed siderurgical aggregate sand 0–2 mm (SSC) to make up for the lack of fines.

Table 1
Physical properties of the aggregates used.

Fraction(mm)	Bulk density [g/cm^3]	Apparent density [g/cm^3]	SSD density [g/cm^3]	Water absorption [% wt.]	Porosity[% vol.]
LC1	2.65	2.76	2.69	1.6	4.2
LC2	2.67	2.78	2.71	1.4	3.7
LS1	2.67	–	–	–	–
SC1	3.84	3.98	3.88	0.9	3.6
SC2	3.82	4.08	3.88	2.1	7.9
SS1	3.87	–	–	–	–
SS2	3.88	–	–	–	–
MC1	4.76	5.05	4.82	1.2	5.7
MS1	4.76	5.00	4.83	1.0	4.8

Table 2
Concrete mix proportions (kg/m^3).

Component	LLC	SLC	SSC	MMC
CEM	340	340	340	340
Water	160	160	160	160
LC1	284	–	–	–
LC2	662	–	–	–
LS1	946	776	–	–
SC1	–	722	722	–
SC2	–	484	484	–
SS1	–	443	443	–
SS2	–	–	1155	–
MC1	–	–	–	1662
MS1	–	–	–	1801
Superplasticizer	3.4	3.4	3.4	3.4
w/c	0.47	0.47	0.47	0.47

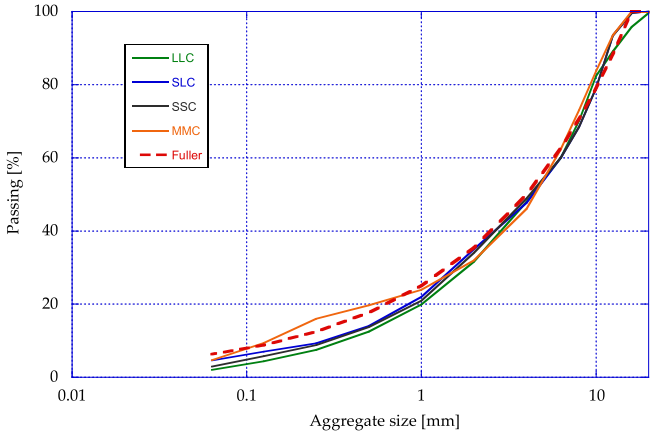

Fig. 1. Grading distribution of the designed mixes.

• A concrete mix with fine and coarse fractions of magnetite aggregates (MMC).

Fig. 1 shows the grading distribution of the 4 mixes.

2.2. Physical and mechanical characterization of concrete

The consistency in the fresh state was determined by means of the slump test in accordance with EN 12350–2 [45] and the occluded air volume was determined in accordance with EN 12350–7 [46]. Regarding the physical properties of the hardened concrete at 28 days, the bulk (D_b), apparent (D_a) and saturated surface dry (D_{ssd}) densities were obtained, following the indications of UNE-EN 12390–7 [47]. The accessible porosity and the water absorption coefficient were also determined in accordance with UNE 83,980 [48].

Regarding the mechanical properties at 28 days, the compressive strength (f_c) was obtained on 5 cubic specimens of 100 mm in accordance with EN 12390–3 [49], using a universal servo-hydraulic press of 2500 kN capacity and 5 kN/s. The secant elastic modulus in compression (E) was determined in accordance with EN 12390–13 [50], using 3 standard cylindrical test specimens (150x300 mm) capped with sulfur on their upper faces and fitted with 120 mm long and 120 Ω strain gauges, using method B. The tensile splitting strength (f_{ct}) was determined on 3 standard cylindrical specimens in accordance with EN 12390–6 [51], using a universal servo-hydraulic press of 2500 kN capacity and a load application speed of 3.5 kN/s.

2.3. Concrete combined hydrogen and elemental composition

Light nuclei, especially hydrogen, are especially effective at attenuating fast neutrons. In concrete, the main (and almost the only) contributor of H is the hydrated CEM, so its quantification is very important when performing simulations, because the elemental composition is the main input. The proportions of each hydration product for ordinary Portland CEM are 50–60% of CSH ($3CaO{\cdot}2SiO_2{\cdot}3H_2O$), 20–25% of CH ($Ca(OH)_2$) and 15–20% monosulphate ($3CaO{\cdot}Al_2O_3{\cdot}CaSO_4{\cdot}12H_2O$), obtained by hydration reactions [20]:

$$2(3\boldsymbol{CaO{\cdot}SiO_2}) + 6\boldsymbol{H_2O} \rightarrow 3\boldsymbol{CaO{\cdot}2SiO_2{\cdot}3H_2O} + 3\boldsymbol{Ca(OH)_2} \quad (1)$$

$$2(2CaO{\cdot}SiO_2) + 4H_2O \rightarrow 3CaO{\cdot}2SiO_2{\cdot}3H_2O + Ca(OH)_2 \quad (2)$$

$$Al_2O_3{\bullet}3CaO + 2H_2O{\bullet}3CaSO_4 + 26H_2O \rightarrow Al_2O_3{\bullet}3CaO{\bullet}3CaSO_4{\bullet}32H_2O \quad (3)$$

$$Al_2O_3{\bullet}3CaO{\bullet}3CaSO_4{\bullet}32H_2O + 2(3CaO{\bullet}Al_2O_3) + 4H_2O \rightarrow 3(Al_2O_3{\bullet}3CaO{\bullet}CaSO_4{\bullet}12H_2O) \quad (4)$$

Eq. (3) corresponds to the reaction of C3A with water in the presence of gypsum (retarder), forming calcium sulphoaluminate (ettringite). Later, after sulfate depletion, ettringite becomes unstable and becomes monosulphate (Eq. (4)) which is the final hydration product of C3A.

The above stoichiometric relationships enable the abundance of H in the hydrated CEM elemental composition to be found, and therefore the amount of water necessary to hydrate all the phases (effective water). The hypotheses adopted for the calculation of the elemental chemical composition of hydrated Portland are the following:

- A factor of 0.95 was applied, corresponding to the minimum clinker content of a CEM I according to EN 197–1 [44].
- To be on the safe side, a proportion of 60% of CSH, 25% of CH and 15% of monosulphate were considered, minimizing the latter because it is the compound with the highest relative content of H.

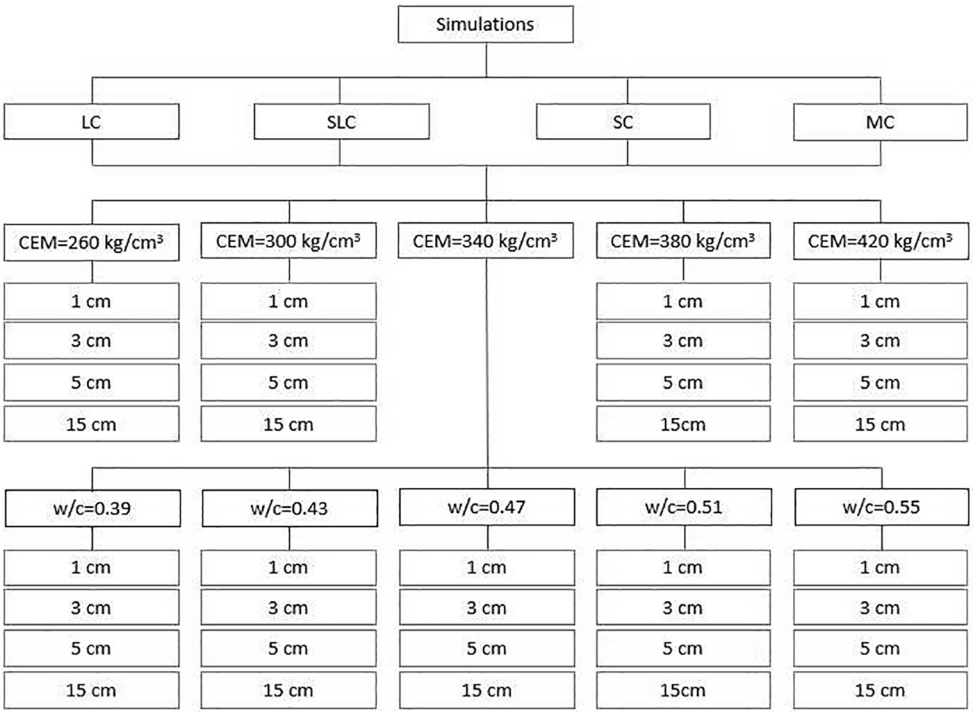

Fig. 2. Experimental program of simulations carried out for both gamma radiation and neutrons.

- Because concrete can operate at temperatures above 100 °C in certain facilities (e.g., spent nuclear fuel containers or in reactors), only the H contributed by bound water (stoichiometric water) was considered.

The chemical composition of the aggregates was obtained from the results obtained by X-Ray Fluorescence (XRF) using a Thermo model ARL-ADVANT-XP brand spectrometer, while the chemical composition of the superplasticizer additive was provided by the manufacturer.

Once the chemical composition of the hydrated cement and the aggregates is obtained and knowing the proportion of aggregates, water and cement in each mix, it is possible to obtain the elemental composition of each mix, as well as its theoretical density.

2.4. Computer simulations

The simulations in this study have two purposes: to collate the experimental results and, once validated, to carry out an analysis of the most critical variables (these also enable the solution of complex transport problems for a wider range of energies). To collate the laboratory results, the geometry of the laboratory was replicated using MAVRIC® (SCALE 6.2.3) computing sequences. The inputs related to the material were the chemical composition and the density of each mixture.

The analysis of critical variables was approached by modifying the w/c ratio and the amount of CEM from 0.39 to 0.55 and from 260 to 420 kg/m^3 respectively, pivoting around the value used in the four mixes (0.47 and 340 kg/m^3). The simulations were carried out in a vacuum with a point detector with an efficiency of 100%. For each mix, nine mix proportions and five thicknesses were simulated, generating a transport

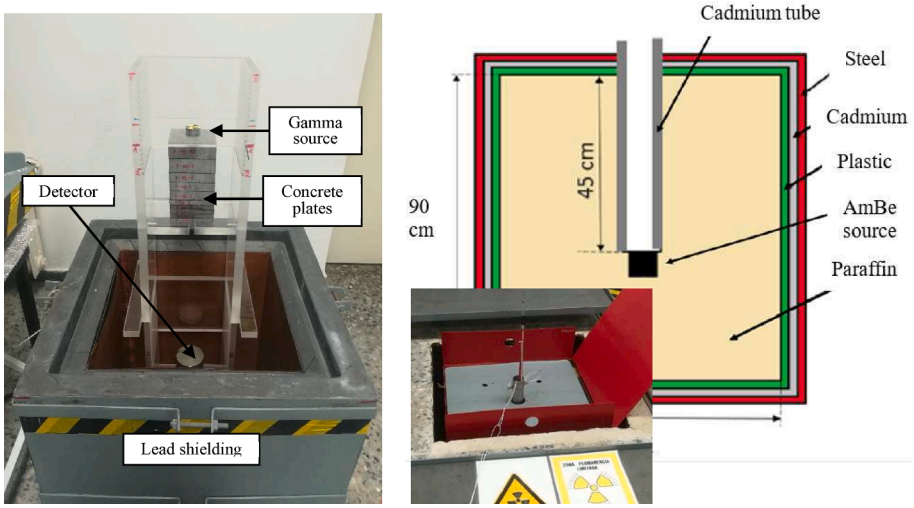

Fig. 3. Experimental set-up for gamma (left) and neutron (right) radiation shielding tests.

Fig. 4. Detail of a complete column of concrete plates (left) and a different series of plates (right).

model for both gamma radiation and neutrons, performing a total of 288 simulations (Fig. 2).

For gamma radiation, photon fluxes were obtained for an energy range of 20 keV-20 MeV and the linear attenuation coefficient μ was obtained by performing a linear fit with the different thicknesses and fluxes obtained for each energy. Neutron fluxes of 0.0005 eV-20 MeV were obtained for neutrons and the attenuation factor (I/I_0) was obtained for a continuous range of thicknesses from 0 to 15 cm. This factor was determined by obtaining Σ through an exponential fit and determining the build-up factor through the fit shown in Eq. (6).

2.5. Validation of simulations through experimental tests

The experimental device was used to validate the results obtained in the simulations (and vice versa). This validation was carried out with the SSC mix and from here on, a experimental program has been proposed with various amounts of CEM and various w/c ratio.

To measure the attenuation capacity with gamma radiation, the methodology consists of placing 100x100 mm^2 concrete plates of different thicknesses between a gamma radiation source and a detector, measuring the intensity of the flow that passes through the material with a detector and comparing it with the intensity when there is no concrete. Using the well-known exponential Lambert's Law [5] the linear attenuation coefficient μ (cm^{-1}) can be established knowing the initial intensity (I_0), the remaining intensity (I) and the thickness of the concrete plate:

$$I = I_0 e^{-\mu \cdot l} \tag{5}$$

To characterize a wide range of photon energies, different sources of gamma radiation were used. The isotopes used were ^{137}Cs (662 keV and $7.2{\cdot}10^5$ Bq), ^{60}Co (1170, 1330 keV and $3.4{\cdot}10^4$ Bq), ^{22}Na (1280 keV and $2.6{\cdot}10^5$ Bq) and ^{207}Bi (570 keV, 1064 keV and $4.9{\cdot}10^4$ Bq). The detector used was a NaI (Tl) scintillator detector (76–100% efficiency for the evaluated energy range) connected to a multichannel analyzer (MCA) and a computer. The experimental set-up is shown in Fig. 3 left.

To measure the neutron attenuation capacity, 40 mm diameter cylindrical concrete plates (Fig. 4) of different thicknesses were used (the total length is 15 cm), placed between the source and the detector. Neutron attenuation does not occur in a purely exponential way (as occurs with photons) due to the influence of neutrons scattered through the shield and in the air until they hit the detector. This effect is corrected by applying a factor or build-up (Δ), which enables the neutron cross-section Σ (cm^{-1}) to be calculated based on the thickness (x), the initial neutron flux (Φ_0) and the final neutron flux (Φ) as shown [52]:

$$\Phi(x) = \Phi_0(1 + \Delta(\Sigma x)^2)e^{-\Sigma x} \tag{6}$$

The neutron source used is Am-Be, and it is located at the bottom of a cadmium tube that acts as a collimator (this tube is coated with paraffin). When ^{241}Am (111 GBq of activity) comes into contact with ^{9}Be, a neutron flux of $6.6{\cdot}10^6$n/s is generated with an average energy of 4 MeV and maximum energy of about 10 MeV. The detector consists of a LiF fluoride sheet enriched in ^{6}Li (whose efficiency was analyzed in [53]). The detector can detect only one of the two particles generated in the interaction of a neutron with concrete (a tritium isotope or an alpha particle) since both describe opposite directions.

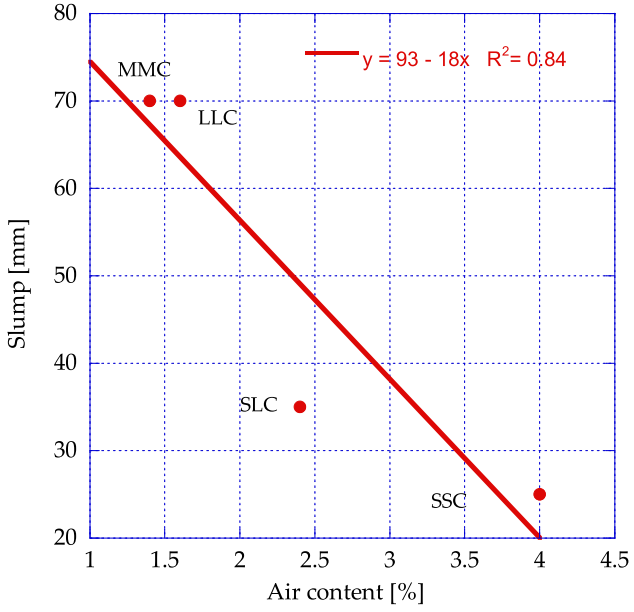

Fig. 5. Fresh properties of concrete: correlation between slump and air content.

3. Results and discussion

3.1. Physical and mechanical characterization of concrete

Fig. 5 shows the average slump values obtained for each of the 4 mixes produced. It can be seen that greater settlements are obtained for mixes that use limestone aggregates and magnetite. This is due to the shape of the limestone and magnetite aggregates, whose shape tends to be spheroidal, without large edges and without planar or flaky particles, which reduces the friction between layers and thus the shear yield stress (Fig. 6).

Fig. 5 also shows the air content of each of the mixes manufactured. A higher air content is observed for mixes that have obtained a lower slump and vice versa. This can be explained because the shape of the siderurgical aggregates is more cavernous than that of natural aggregates, caverns that are filled with paste, requiring a higher volume of paste and thus leaving a greater volume of voids due to a hypothetical loss of compactness of the concrete.

The importance of the vibrating operation on the specimens containing siderurgical aggregates is highlighted, always considering that an excess of vibration can cause the segregation of the siderurgical aggregates towards the bottom of the specimens.

Table 3 shows the physical properties with their standard deviations of the four mixes manufactured. It is observed that the bulk density of the SLC mix is 20% higher than that of the LLC mix, a value that amounts to almost 30% for the SSC mix and 40% for the MMC mix. All mixes except the limestone control concrete exceed 2600 kg/m^3 [54], which is the density above which a high-density concrete is conventionally considered.

The porosity of all the mixes is similar, around 7%. These results show that the concrete vibrating task has been extremely effective with the SLC and SSC mixes, highlighting the importance of this action for

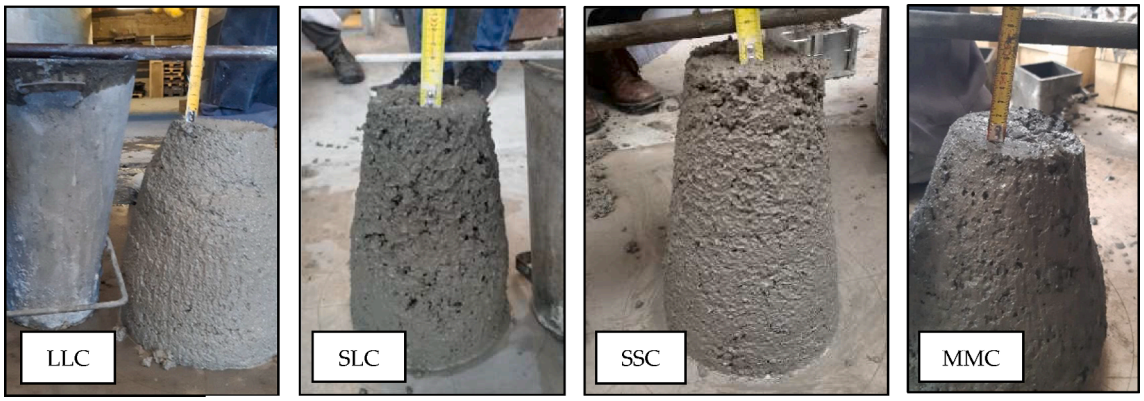

Fig. 6. Slump of the different mix proportions.

Table 3
Physical properties of the mixes produced.

Mix	Bulk density [g/cm^3]	Apparent density [g/cm^3]	SSD density [g/cm^3]	Porosity [% Vol.]	Absorption [% wt.]
LLC	2.34 ± 0.03	2.52 ± 0.03	2.41 ± 0.03	6.97 ± 0.28	2.98 ± 0.14
SLC	2.93 ± 0.02	3.14 ± 0.02	3.05 ± 0.02	6.83 ± 0.16	2.33 ± 0.06
SSC	3.25 ± 0.01	3.47 ± 0.03	3.31 ± 0.02	6.17 ± 0.45	1.90 ± 0.13
MMC	3.93 ± 0.03	4.30 ± 0.02	4.03 ± 0.03	7.72 ± 0.39	1.95 ± 0.12

Table 4
Mechanical properties of the mixes produced.

Mix	f_c [MPa]	E [GPa]	f_{ct} [MPa]
LLC	62.90 ± 6.22	41.25 ± 0.31	3.54 ± 0.19
SLC	89.45 ± 3.15	53.48 ± 1.05	4.12 ± 0.16
SSC	110.39 ± 0.82	58.61 ± 0.64	4.79 ± 0.32
MMC	67.80 ± 2.33	46.81 ± 0.73	3.21 ± 0.23

Table 5
Chemical composition of hydrated Portland cement.

Element	CSH	CH	Monosulphate	Total
O	26.67%	10.27%	8.06%	45.00%
Ca	20.00%	12.84%	3.67%	36.50%
Si	9.33%	0.00%	0.00%	9.33%
Al	0.00%	0.00%	1.24%	1.24%
S	0.00%	0.00%	0.73%	0.73%
H	1.00%	0.64%	0.55%	2.19%

any mix that incorporates siderurgical aggregates.

The angular shape and stiffness of the siderurgical aggregates give the mixes a better quality of the paste-aggregate ITZ [28], which improves its mechanical properties. Similar values of compressive strength were achieved in the LLC (reference) and MMC mixes, but these were 42% and 75% higher in the SLC and SSC mixes, respectively (Table 4). The elastic modulus of the four mixes is analogous to the compressive strength, but the variation between mixes is less.

3.2. Concrete combined hydrogen and elemental composition

Using the calculation process described in the methodology, the composition of the hydrated Portland cement is shown in Table 5.

According to Table 5, the estimated combined hydrogen is 2.19% by weight, obtaining hydration water of 19.73% by weight of the CEM (w/c effective ratio). This means that only 20% of the mixing water was used to hydrate the concrete. The remaining 80% was not considered in the simulations because it was assumed that these concretes will work at service temperatures in which the free water evaporates.

Table 6
Chemical composition of the aggregates used.

Element	Siderurgical aggregates	Limestone aggregates	Magnetite aggregates	Additive
Si	4.80%	0.00%	1.91%	0.00%
O	33.69%	47.96%	28.67%	30.00%
Al	3.16%	0.00%	0.38%	0.00%
Fe	30.15%	0.00%	66.28%	0.00%
Mn	4.43%	0.00%	0.00%	0.00%
Mg	4.11%	0.00%	0.00%	0.00%
Ca	15.30%	40.05%	1.82%	0.00%
Na	0.01%	0.00%	0.23%	5.00%
Ti	0.29%	0.00%	0.17%	0.00%
P	0.12%	0.00%	0.51%	0.00%
S	0.10%	0.00%	0.03%	1,00%
V	0.20%	0.00%	0.00%	0.00%
Cr	3.64%	0.00%	0.00%	0.00%
C	0.00%	11.99%	0.00%	64.00%

Table 7
Chemical composition of the four starting mixes.

Element	LLC	SLC	SSC	MMC
O	47.47%	39.32%	35.23%	30.50%
Ca	39.99%	25.70%	18.53%	5.99%
Si	1.28%	3.82%	5.09%	2.46%
Al	0.25%	2.03%	2.92%	0.49%
Fe	0.26%	17.64%	26.35%	59.15%
S	0.19%	0.21%	0.22%	0.14%
K	0.06%	0.05%	0.04%	0.19%
Mg	0.10%	2.46%	3.64%	0.06%
Ti	0.01%	0.18%	0.26%	0.01%
C	9.96%	3.41%	0.13%	0.11%
H	0.40%	0.33%	0.29%	0.24%
Na	0.01%	0.01%	0.01%	0.21%
Mn	0.00%	2.56%	3.84%	0.00%
P	0.00%	0.07%	0.10%	0.45%
V	0.00%	0.12%	0.17%	0.00%
Cr	0.00%	2.10%	3.16%	0.00%
TOTAL	100.00%	100.00%	100.00%	100.00%

The chemical composition of the aggregates and additive used are shown in Table 6.

The chemical composition of the mixes obtained from the mix proportions is shown in Table 7. With these proportions, the proportion by weight of each component is obtained. With the composition of the hydrated CEM, the aggregates and the additive, the chemical composition of the four starting mixes and all the mixes can be calculated.

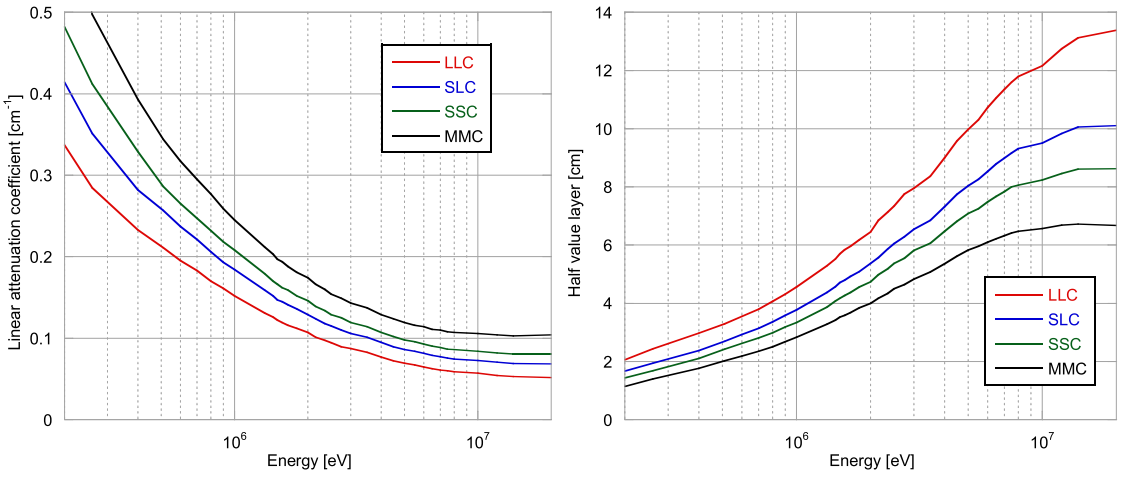

Fig. 7. Linear attenuation coefficient (left) and half value layer (right) for the four main mixes.

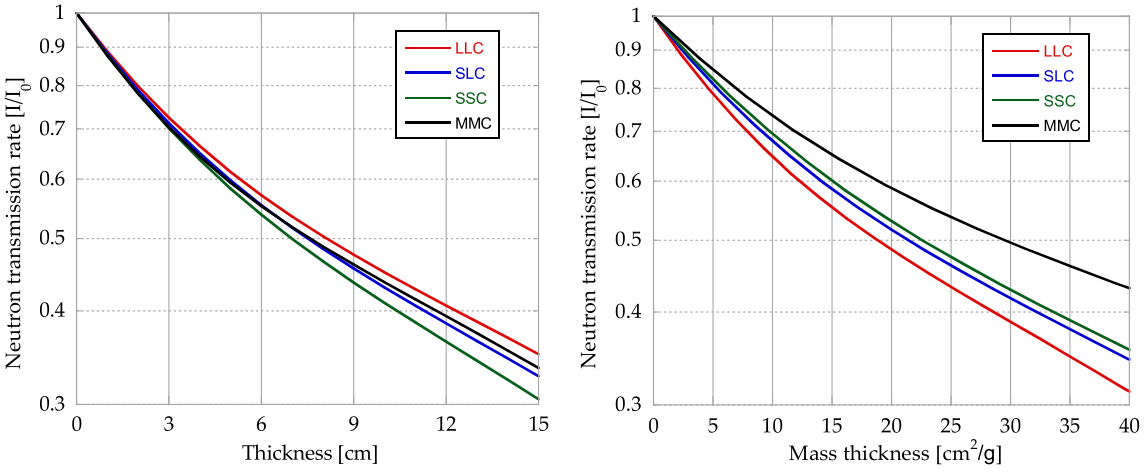

Fig. 8. Neutron transmission rate (I/I_0) for the four main mixes.

3.3. Computer simulations

3.3.1. Effect of the aggregates on shielding capacity

The four initial mixes developed (340 kg/m^3 and w/c = 0.47) have the same volume of aggregates, so their comparison indicates the behavior of each type of aggregate. Fig. 7 (left) shows the linear attenuation coefficient (μ) for the four mixes as a function of energy. Between 1 and 10 MeV the SLC shows a μ 24% on average higher than the control mix (LLC), while in the case of the SSC mix, this value rises to 41%, demonstrating a directly proportional positive impact of the slags at the

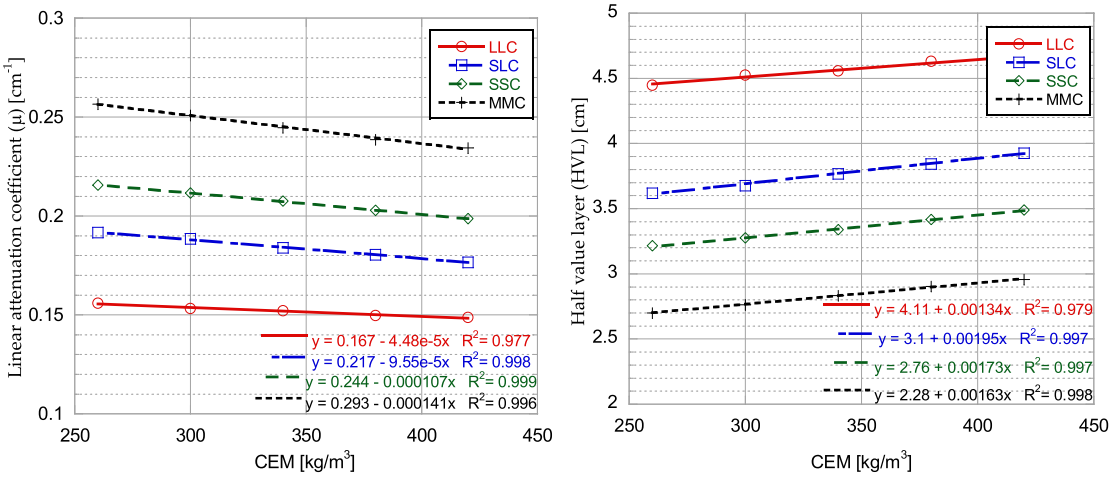

Fig. 9. Effect of the amount of cement on μ and HVL for energies of 1 MeV.

level of replacement of the aggregate. On the other hand, the MMC mix shows a μ 71% higher than the LLC mix and only 21% higher than the SSC mix, which shows the potential of this by-product for radiation shielding purposes. From 10 MeV the linear attenuation coefficient tends to stabilize for all mixes.

Fig. 7 (right) shows the half-value layer (HVL) or thickness for which 50% of the incident flow is attenuated for the four mixes as a function of energy. The average HVL in the energy range of 1–10 MeV for the SLC mix is 19% lower than that of the LLC mix, while for the SSC mix, this value rises to 28%, with the consequent saving of material. On the other hand, the MMC mix shows an HVL 40% lower than the LLC and 17% lower than the SSC. Considering the density of each mix, the results obtained show agreement with the data obtained by Sayed and Bourham [55] for mixes with magnetite and lead oxides.

With the SSC mix, a notable thickness saving with respect to the LLC of almost 30% is obtained, but a slightly higher material expenditure is required when compared to the MMC. In the latter case, the low (or zero) cost of the siderurgical aggregates compensates for the slight difference in shielding capacity.

Fig. 8 (left) shows neutron transmission as a function of concrete thickness of the four simulated mixes. A higher neutron transmission rate corresponds to less efficient concrete. It can be seen that the difference between mixes is greater when the thickness of the specimen is greater; for thicknesses less than 50 mm, the differences are very small, but they are palpable for thicknesses of 10–15 cm. For thicknesses of 15 cm, the least efficient concrete at attenuating neutrons corresponds to the LLC mix, while the most effective is the SSC mix, showing 17% higher attenuation efficiency. A priori, it was possible to think that the higher content of C and O could give the LLC mix greater attenuation; however, the higher density of the SSC mix seems not only to compensate for this effect but also to give it an advantage. The SLC mix, which has an intermediate chemical composition between LLC and SSC, shows an intermediate attenuation between both mixes. On the other hand, the MMC mix shows very similar behavior to the SLC since the high iron content reduces the relative presence of O, an effect that is offset by the high density of the magnetite aggregates.

To ignore the effect of density, I/I_0 is usually represented as a mass thickness function (cm^2/g). In Fig. 8 (right), this relationship is plotted, and it can be observed that the mixes with a higher content of light elements display better neutron attenuation, while the mix with magnetite shows the worst shielding efficiency and the mixes that incorporate siderurgical aggregates display intermediate behavior.

3.3.2. *Effect of the amount of cement on shielding capacity*

As already mentioned, CEM plays an important role in the radiological behavior of concrete, since in a hydrated form, it is a source of the contribution of H. Fig. 9 (left) shows the variation of μ with the amount of CEM used, for each mix analyzed. Larger μ corresponds to concrete mixes that are more effective at attenuating photons. The behavior for an energy of 1 MeV was analyzed, as this is a typical energy used in these cases.

For the LLC reference mix, the μ loss is 3.1% for every 100 kg of CEM added; for the SLC mix, the loss amounts to 4.9%, and for the SSC and MMC mixes, the loss increases to 5.8% for every 100 kg of CEM. These losses are because the CEM is less dense than any of the aggregates used, affecting the densest mixes in a more pronounced way. Fig. 9 (right) shows the evolution of HVL; as this value depends only on μ, the increases in thickness of the half-value layer are of the same type as the losses in terms of linear attenuation. As for the comparison between different mixes, with respect to the reference concrete, the SLC mix displays a 17% higher average μ, the SSC mix a 27% higher μ, and in the case of the MMC mix, this amount rises to 38%. This effect is solely caused by the difference in density among the different types of concrete.

Fig. 10 (left) shows the effect of the amount of CEM on the neutron removal cross-section (Σ) for each mix. It was found that 100 kg of CEM produces a reduction in Σ of 1.3% for the LLC mix, 2.1% for SLC, 1.9% for SSC and 2.5% for MMC. This is inconsistent with the expected results, and this is because the density effect is substantial.

To compare materials, regardless of their density, the concept of mass removal cross-section (Σ/ρ) is commonly used, with units of cm^2/g. In Fig. 10 (right), the effect of the amount of CEM on Σ/ρ is shown, both increasing proportionally. This increase is 2.3%, 2.8%, 3.7% and 4% per 100 kg of CEM for the LLC, SLC, SSC, MMC mixes, respectively.

Regarding the comparison among mixes, it is found that the mix that most attenuates neutrons is the LLC mix, followed by the SLC mix (14% lower), followed by the SSC mix (22% lower), followed by the MMC mix (34 % lower). This can be explained as the mixes that use limestone aggregate contain more light elements (C and O mainly) since the amount of hydrated paste remained constant in the four mixes. It can also be observed that the linear fitting displays excellent agreement, always close to $R^2 = 1$.

When analyzing the behavior of each mix in detail, in the case of gamma radiation, the effect of the amount of CEM was analyzed in the entire simulated energy range (10^5-$2{\cdot}10^7$ eV), and in the case of neutrons, the attenuation (I/I_0) as a function of the thickness was analyzed (a most typical form of analysis).

Fig. 11 shows that μ evolves as a function of the amount of CEM and the energy of the photon beam. The differences between mixes with the same aggregate and different amounts of CEM are very similar to those expressed in Fig. 11 for energies of 10^6 eV. In the evolution of μ with the energy of the photons, it is possible to consider linear behavior (straight

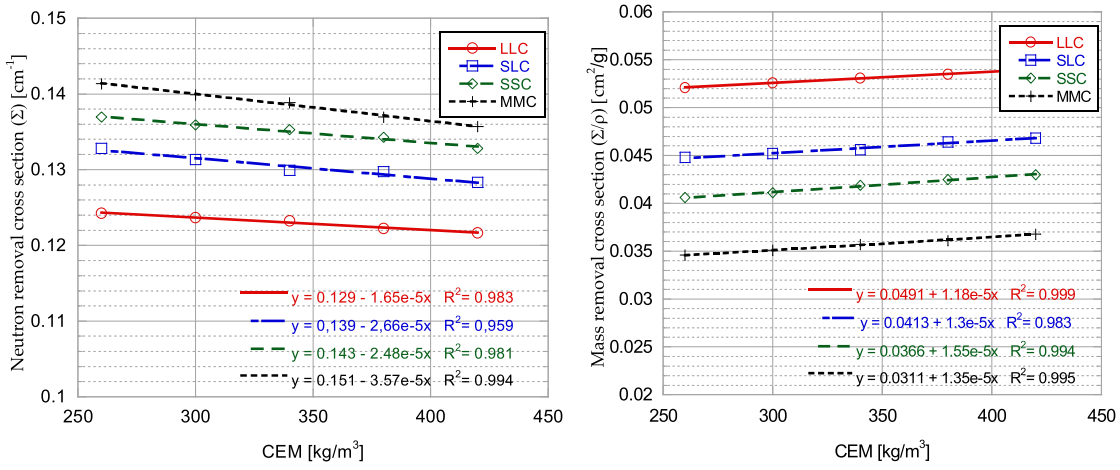

Fig. 10. Effect of the quantity of cement on Σ and on Σ/ρ.

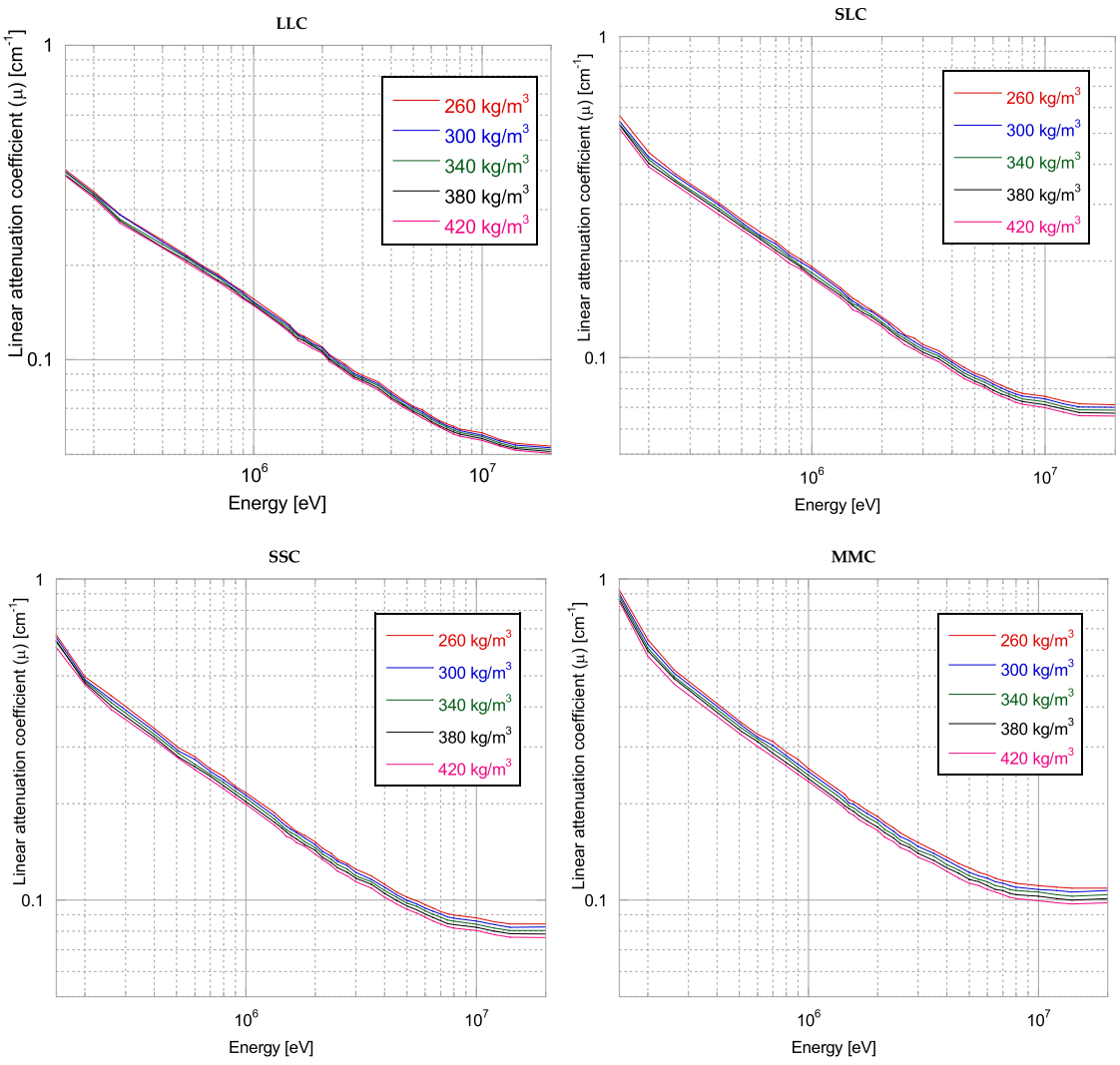

Fig. 11. Effect of the amount of cement on μ as a function of the photon energy.

line in double logarithmic axis) between $1.2{\cdot}10^5$ and 10^7 eV for all the mixes analyzed, which coincides with the energy region where the Compton effect predominates (~1–10 MeV) for elements of low and intermediate atomic numbers.

Comparing the 4 mixes, the relationship between the drop in μ and the type of aggregate used can be established. For the LLC mix, a loss of 90.2% of μ (between 10^5 and $2{\cdot}10^7$ eV) was found for all the quantities of CEM analyzed; for the SLC mix, this drop amounts to 91.7%, 91.4% for the SSC mix and 93.3% for the MMC mix, given that the higher the density of the concrete, the greater the loss of density due to the incorporation of more CEM. Finally, it should be noted that the linear attenuation coefficient tends to stabilize for energies close to 10 MeV, obtaining stabilized average values of μ of 0.052 cm^{-1} (LLC), 0.068 cm^{-1} (SLC), 0.080 cm^{-1} (SSC) and 0.104 cm^{-1} (MMC).

Fig. 12 shows the evolution of I/I_0 as a function of the amount of CEM and the mass thickness. The differences are so small that an obvious change among the different amounts of CEM used cannot be distinguished in a graph where a large range of data is identified (Fig. 12 left). To facilitate the visualization, values of mass thickness between 6 and 8 cm^2/g have been magnified (region captured by the magnifying glass), and have been shown in Fig. 12 (right).

For all mixes, increasing the amount of CEM decreases the neutron transmission rate, a lower level of neutron flux reaching the detector. This improvement in shielding is produced by the combined H provided by the hydrated CEM phases. The effect of the amount of CEM depends on the mass thickness, being greater for higher thicknesses.

Within the range of mass thicknesses of 6–8 cm^2/g for the LLC mix, it is possible to reduce the I/I_0 by 0.41% for every 100 kg of additional CEM used, for the SLC mix, the amount is 0.48%, for the SSC mix it rises to 0.56% and for the MMC mix it is 0.64% per 100 kg of CEM. The reason why denser mixes undergo an additional effect of CEM is because they have a lower initial amount of light elements.

3.3.3. *Effect of the w/c ratio on shielding capacity*

Minimizing the w/c ratio is necessary to maximize the concrete's strength and durability, with the trade-off affecting the consistency in the fresh state. However, this parameter also affects the shielding properties of the concrete, while increasing or reducing the mixing water means increasing or reducing the proportion of the other components of the concrete. In the calculation hypothesis, it must be emphasized that unbound water (37–52% wt. of total water, according to the w/c used) was not considered because these concrete mixes can work at high temperatures that favor evaporation, which can be considered to be on the safe side.

Fig. 13 (left) shows the effect of the w/c ratio on μ for photon energies of 1 MeV. A loss was found in μ of 3.2% for LLC, 4.3% for SLC, 3.5% for SSC and 3.9% for MMC for each increase of 0.1 in the w/c ratio. These losses are due to the loss of density derived from incorporating

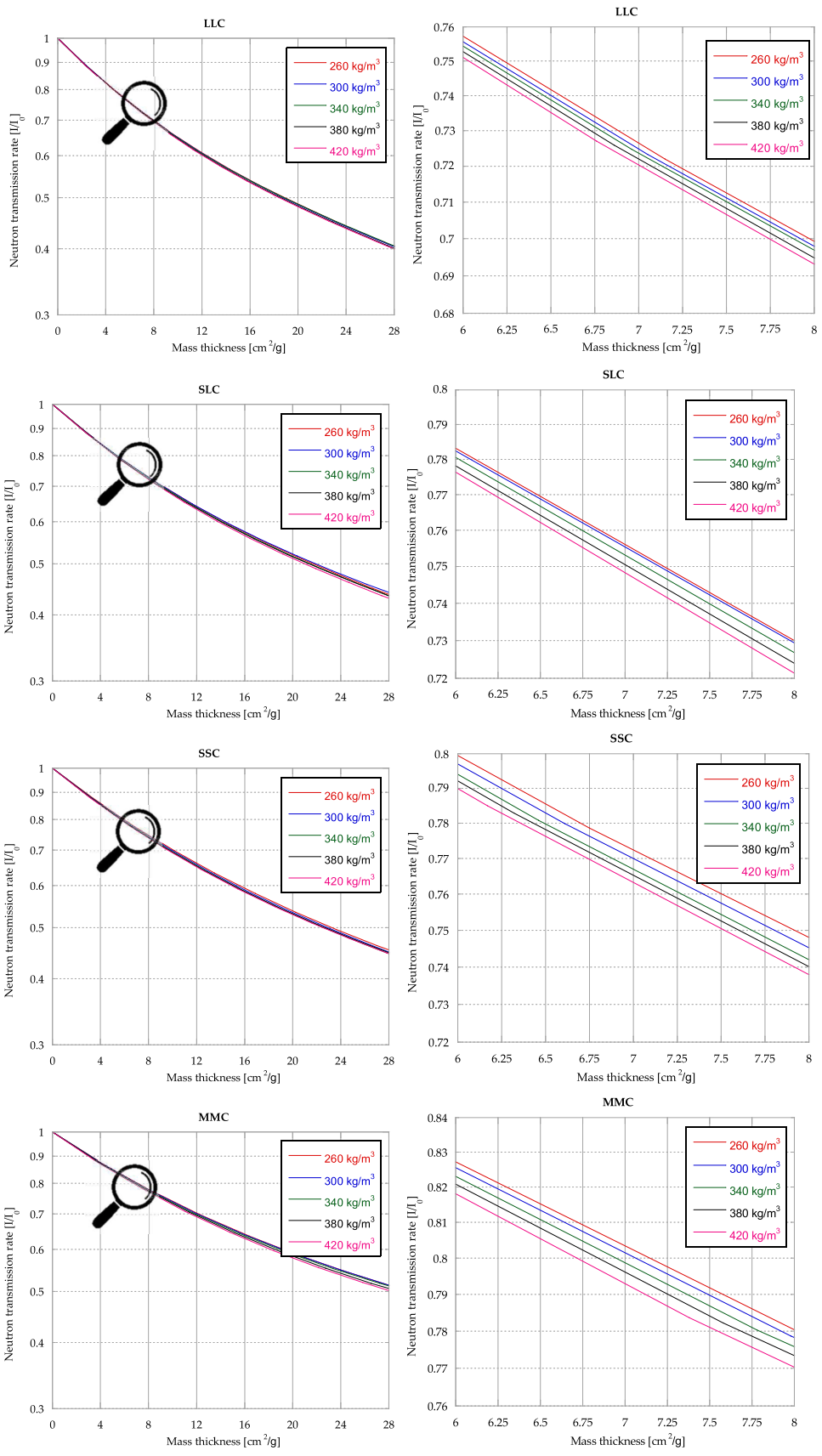

Fig. 12. Effect of the amount of cement on I/I_0 as a function of the mass thickness.

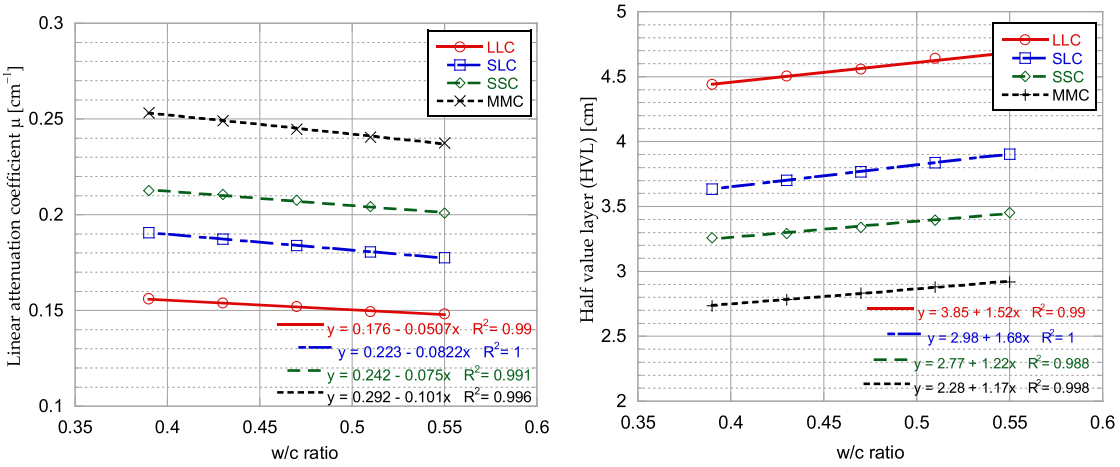

Fig. 13. Effect of the w/c ratio on μ and HVL for energies of 1 MeV.

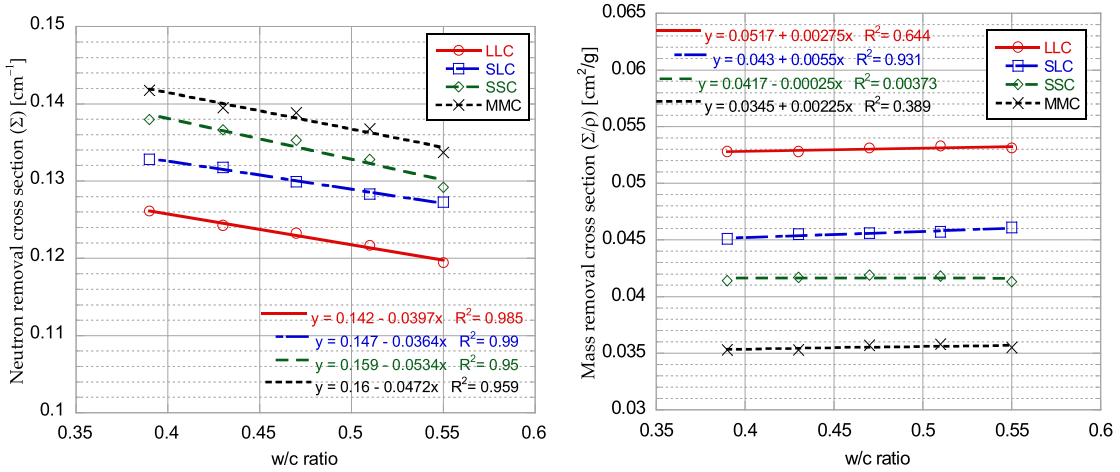

Fig. 14. Effect of the w/c ratio on Σ and on Σ/ρ.

more water per cubic meter, with the consequent loss of volume of CEM and aggregates. In the comparison among the different concrete mixes, it was found that, on average and with respect to the LLC mix, μ increases by 17 for the SLC mix, 27% for the SSC mix and 38% for the MMC mix, which indicates better behavior for denser concrete at any w/c ratio.

In Fig. 13 (right) the behavior against gamma radiation is expressed in terms of HVL, which is proportional to the w/c ratio. The average increases in HVL are the same as the losses obtained for μ, expressed in the thickness of material necessary to reduce radiation intensity by half.

Fig. 14 (left) shows the effect of the w/c ratio on Σ. It can be observed that Σ decreases with the increase of the w/c ratio for all concrete mixes. A loss in Σ was found for each 0.1 increase in the w/c ratio of 6.9% for the LLC mix, 6.8% for the SLC mix, 7.0% for the SSC mix and 6.7% for the MMC mix. When not incorporating more light elements when increasing the w/c ratio (a hypothesis that free water evaporates), it seems clear that the decrease in Σ is only due to the loss of density of the concrete. Comparing the different mixes, an increase in Σ of 5.4% was found for the SLC mix, 8.5% for the SSC mix and 11.0% for the MMC mix with respect to the LLC control mix. Theory suggests that concretes with a higher presence of O and C should show better behavior, which occurs when considering the density of the concrete to establish the materials behavior. This density effect can again be ignored, calculating the mass removal cross-section (Σ/ρ) to evaluate the real effectiveness of the material in attenuating fast neutrons.

Fig. 14 (right) shows the evolution of Σ/ρ with the variation of the w/c ratio. As the chemical composition of the mixes does not vary with the variation of the w/c ratio (the additional water from increasing w evaporates), it is found that Σ/ρ does not vary (slope of the linear fits is close to 0). In the comparison among mixes with different aggregates, regardless of the w/c ratio, with respect to the LLC mix, a lower Σ/ρ was found of 14% for the SLC, 21.5% for SSC and 33% for MMC, due to the high relative concentration of O and C in mixes that incorporate limestone aggregates and the difference in relative O content among mixes that do not incorporate limestone aggregates (SSC and MMC). Therefore, it is established that the variation of the w/c ratio for the calculation hypothesis used only affects the attenuation of gamma radiation.

Fig. 15 shows the effect of the w/c ratio on μ as a function of the photon energy. The variation of μ with w/c for the entire energy spectrum analyzed (10^5-$2{\cdot}10^7$ eV) is very similar to that at 1 MeV. On the other hand, the same previously commented effect is observed for mixes with a different amounts of CEM; there is a zone between approximately $1.2{\cdot}10^5$ and 10^7 eV where the attenuation varies proportionally with the energy due to Compton interaction.

In the comparison among the four mixes, between 10^5 and $2{\cdot}10^7$ eV, the LLC mix lost 90.0% of μ, the SLC mix 91.8%, the SSC mix 91.4% and the MMC mix 93.2%, the loss being higher for the densest mixes. Likewise, the average values for which μ stabilizes for energies of 10 MeV are 0.057 cm^{-1} for the LLC mix, 0.073 cm^{-1} for the SLC mix, 0.084 cm^{-1} for the SSC mix and 0.103 cm^{-1} for the MMC mix.

After analyzing the four graphs, it can be concluded that an increase

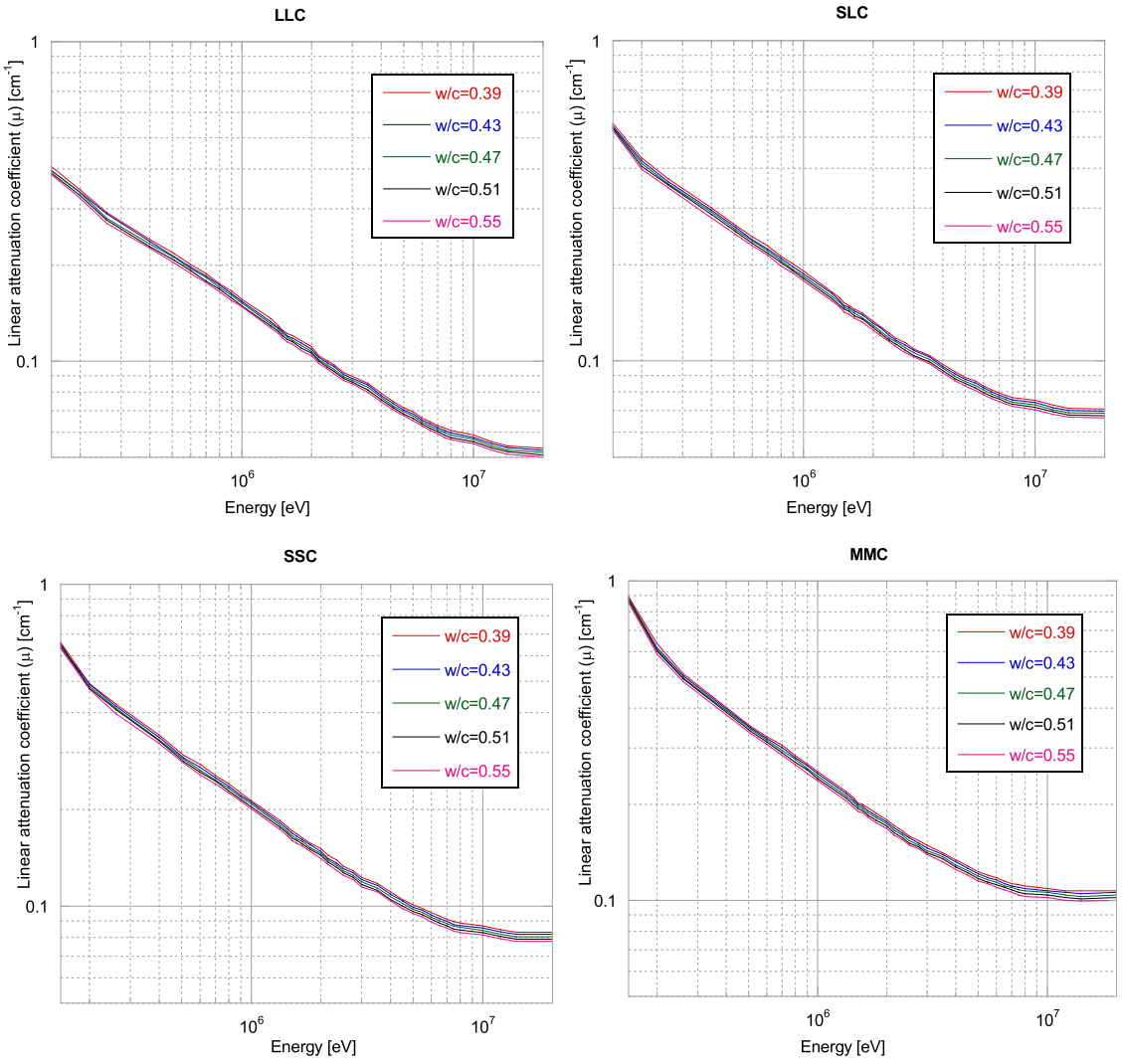

Fig. 15. Effect of the w/c ratio on μ as a function of the photon energy.

in w/c negatively affects the linear attenuation coefficient for all mixes and in a similar way, although the densest mixes show higher curves.

Fig. 16 shows the evolution of I/I_0 as a function of the mass thickness and the w/c ratio. In Fig. 16 (left), the evolution for a wide range of mass thicknesses is shown, where it can be seen that the variation is negligible. In Fig. 16 (right), the zoom of the evolution of I/I_0 is shown for mass thicknesses between 6 and 8 cm^2/g, where no palpable variation is observed either.

As already analyzed for Σ/ρ, a variable that considers the range of thicknesses, I/I_0 does not vary because the chemical composition of the concrete does not change when the w/c ratio is varied. After all, unbound water is assumed to evaporate and also there is density compensation. Therefore, it could be concluded that, although the variation of the w/c ratio has a very slight effect on the attenuation of gamma radiation, the effect is negligible on the attenuation of neutrons.

3.3.4. Other relationships

There are several works obtaining correlations between density and μ after the characterization of various concretes in the literature. Pomaro [56] performed a linear fit for specimens subjected to 1.25 MeV, obtaining μ=0.0542x + 0.0098. Şensoy [57] analyzes specimens subjected to 662 keV (one of the peaks of the ^{137}Cs energy spectrum) obtaining a fit of μ=0.0767x + 0.0189. Fig. 17 (left) shows the correlation between density and μ and the fit obtained for various typical energies. A linear fit can be seen in this Fig. 17 (left), but also a very close correspondence with the slopes of the fits obtained by the aforementioned authors [56,57].

As one of the main concerns in the sector of shielding structures is the content of H, an analysis of the effect of H on Σ/ρ has been carried out for each mix. In Fig. 17 (right), it can be seen that a greater amount of H produces a notable increase in Σ/ρ. This increase is slightly more noticeable in denser mixes.

Table 8 shows the necessary reduction in w/c and the necessary reduction in CEM to increase the linear attenuation coefficient by 0.01 cm^{-1}. It can be seen that reducing the w/c is twice as effective for the LLC mix as for the MMC mix. Likewise, a greater reduction in the amount of CEM is necessary for the lighter mixes because the CEM density is more similar to that of the light mixes.

Table 9 shows the variations of w/c and the amount of CEM that produce the same variation of μ for each mix. Two matches are shown; the first is for each variation of 0.1 of the w/c ratio, the second is for each variation of 100 kg/m^3 of CEM.

3.4. Validation of simulations through experimental tests

The causes that hinder good agreement between simulations and experimental tests are derived from considering concrete as a totally homogeneous material. One of these causes is porosity, which greatly

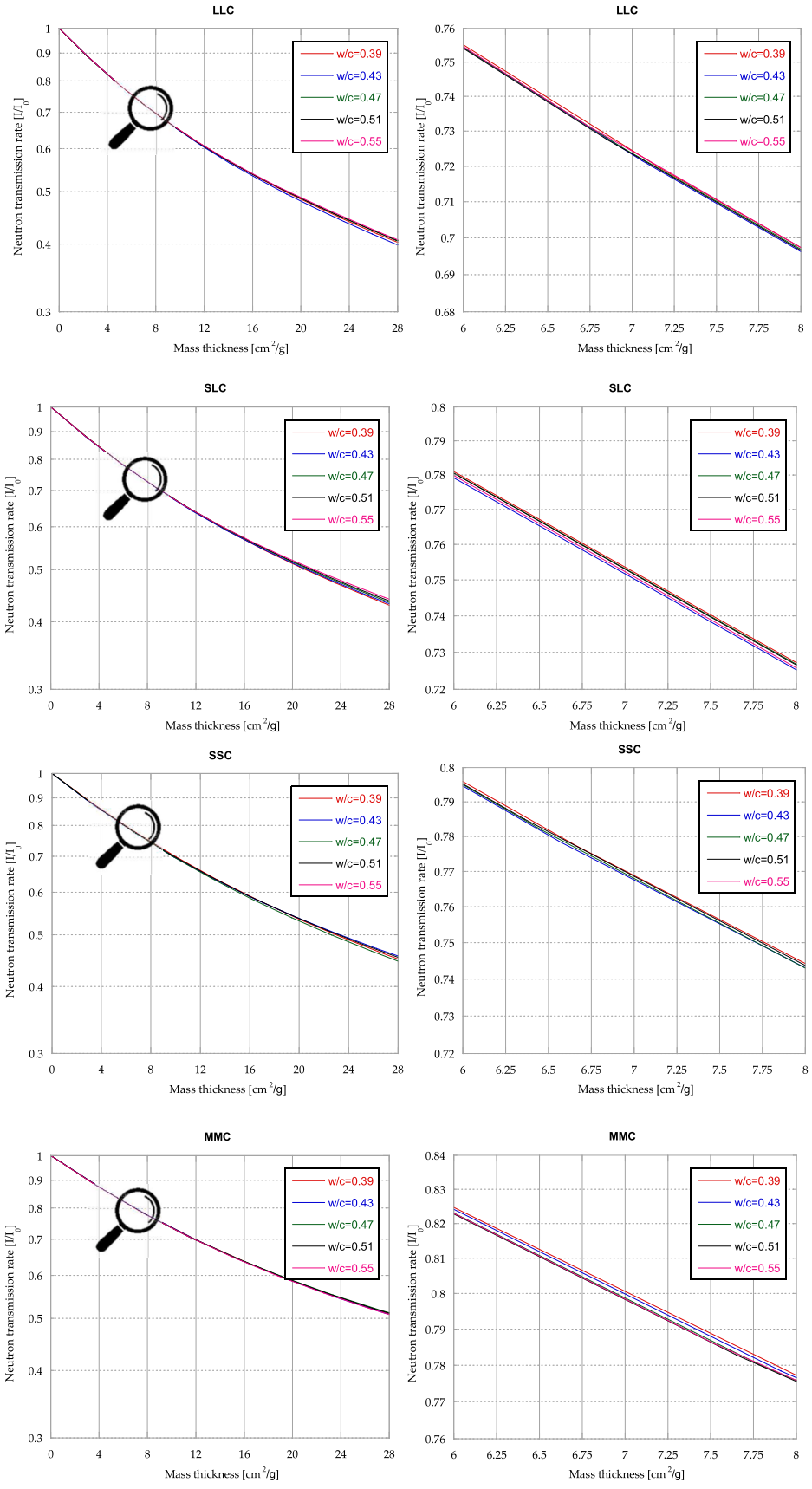

Fig. 16. Effect of the amount of cement on I/I_0 as a function of thickness.

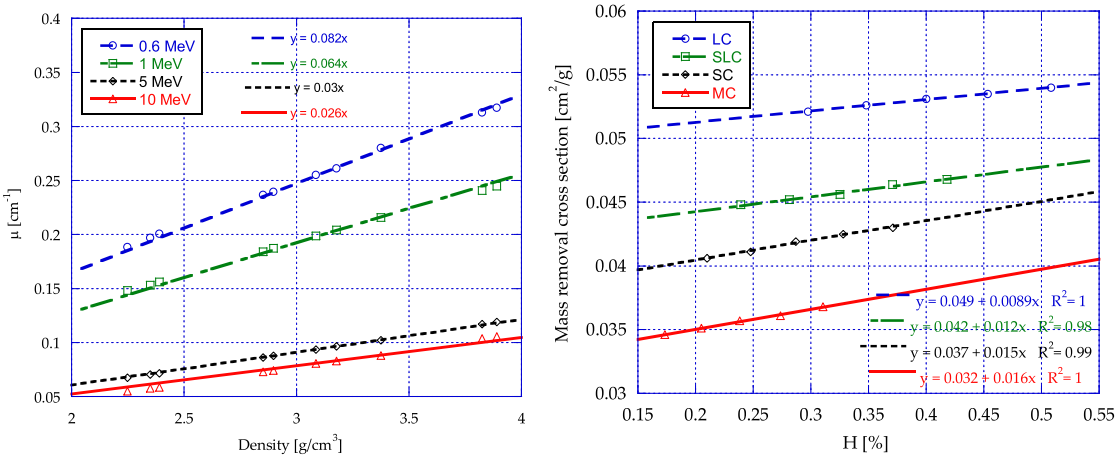

Fig. 17. Correlation between density (left) and μ and effect of the amount of H on Σ/ρ (right).

Table 8
Reduction in w/c and in kg/m^3 CEM to increase μ by 0.01 cm^{-1}.

Mix	Decrease in w/c	Decrease in kg/m^3 CEM
LLC	0.20	218.0
SLC	0.12	104.0
SSC	0.13	93.6
MMC	0.10	70.4

Table 9
Correspondence between variation of w/c and variation of kg/m^3 of CEM to achieve the same variation of μ.

Mix	Variation in w/c	Variation in kg/m^3 CEM	Variation in w/c	Variation in kg/m^3 CEM
LLC	0.1	109.0	0.09	100
SLC	0.1	86.7	0.12	100
SSC	0.1	72.0	0.14	100
MMC	0.1	70.4	0.14	100

reduces the density of concrete and leads to the creation of micro-zones without shielding [58]. Another important factor is the segregation of aggregates, a common phenomenon with high-density aggregates that influences the attenuation capacity of concrete.

In Fig. 18 (left), the linear attenuation coefficients obtained through simulation with Scale and through the experimental device for the SSC mix are shown. The experimental results show a linear attenuation coefficient between 0.17 and 0.25 cm^{-1} for the range of energies analyzed (~500–1400 keV) and an average total error of 0.44%, comparable with that obtained by other researchers (less than2%) [59] and induced by detector error and exposure time. The total error obtained in the simulations is approximately an order of magnitude lower than the experimental one. The correspondence between linear attenuation coefficients (experimental and simulations) is shown in Fig. 18 (right), where most of the points plotted are within the 95% confidence bounds. The points with the lowest correspondence coincide with the isotopes with the highest energy, namely ^{60}Co (1330 keV) and ^{22}Na (1280 keV). Within the confidence bounds, there is also a line with slope 1 so that good agreement can be established between experimental tests and simulations.

Fig. 19 (left) shows the variation of the neutron attenuation factor (I/I_0) as a function of the thickness of the concrete. A notable dispersion of the experimental data is observed, mainly due to the efficiency of the detector. In any case, the values shown by the simulations fit within the interval generated by the error of the experimental results. Fig. 19 (right) shows the correlation between the experimental results and the simulations, displaying a high degree of correspondence ($R^2 = 0.995$) with a linear fit, where the line with slope 1 fits within the 95% confidence bounds, validating the correspondence.

The validation of the SSC mix simulations with the experimental tests shows that the low porosity of the mixtures of around 6–8% (Fig. 19) and

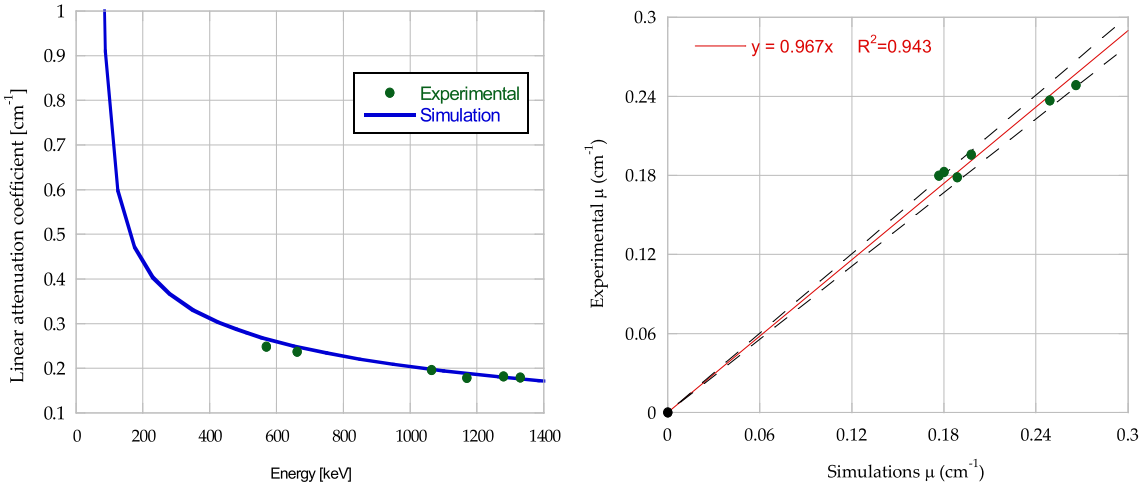

Fig. 18. Linear attenuation coefficient for experimental/simulation tests for the SSC mix (left), and correlation (right).

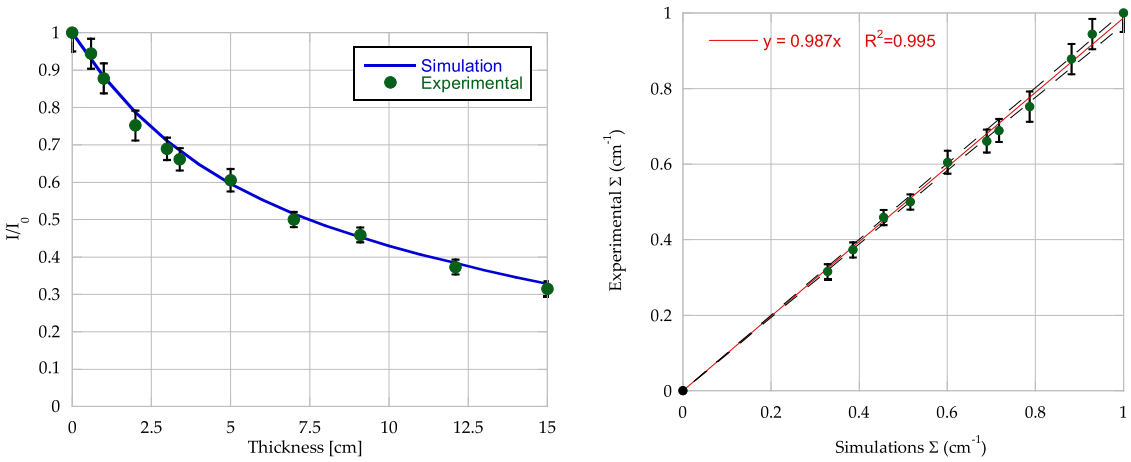

Fig. 19. Neutron attenuation factor (I/I_0) for experimental/simulation for the SSC mix (left), and agreement between removal cross-sections (right).

a low level of segregation, due to the use of a dense paste, enable the theoretical calculation hypothesis to be validated, assuming concrete to be a homogeneous material for the other 36 mixes.

4. Conclusions

In this research, the physical–mechanical response and radiological shielding capacity of concrete with siderurgical aggregates and concrete with limestone and magnetite aggregates were compared, verifying the effect of varying the w/c ratio and the amount of CEM. After analyzing the results, the following conclusions can be drawn:

- A good correlation between slump and air content has been shown, the former increasing as the latter decreasing.
- The angular shape and stiffness of the siderurgical aggregates give the mixes a better quality of the paste-aggregate ITZ, which improves their mechanical properties with respect to limestone and magnetite aggregates. Compressive strength increases 42% and 75% for the SLC and SSC mixes respectively compared to the reference mix.
- With respect to the LLC mix, the HVL was 19%, 28% and 40% less for the SLC, SSC and MMC mixes, respectively. However, the neutron transmission rate (I/I_0) was contrasted by the HVL.
- For every 100 kg of CEM, the loss of μ or HVL was from 3% (LLC) to 6% (MMC) depending on the density of the mix. However, for every 100 kg of CEM the Σ/ρ increased by 2.3%, 2.8%, 3.4% and 4% for the LLC, SLC, SSC and MMC mixes, respectively.
- For every 0.1 increase in the w/c ratio, there was a reduction in μ of approximately 3.2%, 4.3% 3.5% 3.9% for the LLC, SLC, SSC and MMC mixes, respectively. On the other hand, the variation of the w/c ratio did not affect Σ/ρ because the chemical composition of the four mixes is practically the same, since the unbound water is assumed to be evaporated because these concretes tend to work at high temperatures.
- Good agreement between the simulations and the experimental test was confirmed, tanto para μ como para Σ, displaying a high degree of correspondence (R^2 close to 1) with a linear fit, where the line with slope 1 fits within the 95% confidence bounds.
- A linear relationship was found between density and linear attenuation coefficient for all the energies analyzed, contrasting the values by other authors. Likewise, a relationship between H content and mass removal cross-section has been demonstrated.

CRediT authorship contribution statement

P. Tamayo: Data curation, Formal analysis, Writing – original draft. **C. Thomas:** Conceptualization, Data curation, Formal analysis, Funding acquisition, Project administration, Resources, Supervision, Visualization, Writing – original draft, Writing – review & editing. **J. Rico:** Conceptualization, Data curation, Formal analysis, Funding acquisition, Resources, Visualization, Writing – review & editing. **S. Pérez:** Data curation, Formal analysis, Writing – review & editing. **A. Mañanes:** Formal analysis, Funding acquisition, Resources, Supervision, Visualization, Writing – review & editing.

Declaration of Competing Interest

The authors declare that they have no known competing financial interests or personal relationships that could have appeared to influence the work reported in this paper.

Acknowledgments

This research was co-financed by the European Regional Development Fund (ERDF) and the Ministry of Economy, Industry and Competitiveness (MINECO) within the framework of the project RTC-2016-5637-3. The research has been possible thanks to the collaboration of the company INGECID, the department LADICIM (University of Cantabria) the Modern Physics Department of the University of Cantabria and the companies ROCACERO and SIDENOR.

References

[1] K. Singh, S. Singh, A.S. Dhaliwal, G. Singh, Gamma radiation shielding analysis of lead-flyash concretes, Appl. Radiat. Isot. 95 (2015) 174–179.
[2] A. El-Sayed Abdo, Calculation of the cross-sections for fast neutrons and gamma-rays in concrete shields, Ann. Nucl. Energy. 29 (2002) 1977–1988. 10.1016/S0306-4549(02)00019-1.
[3] E. Comission, Horizon 2020 programme, (n.d.). https://ec.europa.eu/programmes/horizon2020/en/area/raw-materials (accessed August 1, 2021).
[4] F. Faleschini, P. De Marzi, C. Pellegrino, Recycled concrete containing EAF slag: environmental assessment through LCA, Eur. J. Environ. Civ. Eng. 18 (2014) 1009–1024.
[5] J. Kazjonovs, D. Bajare, A. Korjakins, Designing of high density concrete by using steel treatment waste, in: 10th Int. Conf. Mod. Build. Mater. Struct. Tech., 2010: pp. 138–142.
[6] M.A. González-Ortega, I. Segura, S.H.P. Cavalaro, B. Toralles-Carbonari, A. Aguado, A.C. Andrello, Radiological protection and mechanical properties of concretes with EAF steel slags, Constr. Build. Mater. 51 (2014) 432–438, https://doi.org/10.1016/j.conbuildmat.2013.10.067.
[7] E.N. 206-1, Concrete - Part 1: Specification, performance, production and conformity, (2008).
[8] C. Thomas, J. Rico, P. Tamayo, F. Ballester, J. Setién, J.A. Polanco, Effect of elevated temperature on the mechanical properties and microstructure of heavy-weight magnetite concrete with steel fibers, Cem. Concr. Compos. 103 (2019) 80–88.

[9] C. Thomas, P. Tamayo, J. Setien, D. Ferreno, J.A. Polanco, J. Rico, Effect of high temperature and accelerated aging in high density micro-concrete, Constr. Build. Mater. 272 (2021), 121920.
[10] O. Gencel, A. Bozkurt, E. Kam, T. Korkut, Determination and calculation of gamma and neutron shielding characteristics of concretes containing different hematite proportions, Ann. Nucl. Energy. 38 (2011) 2719–2723.
[11] Y.-C. Peng, C.-L. Hwang, Development of high performance and high strength heavy concrete for radiation shielding structures, Int. J. Miner. Metall. Mater. 18 (2011) 89–93.
[12] I. Akkurt, A.M. El-Khayatt, The effect of barite proportion on neutron and gamma-ray shielding, Ann. Nucl. Energy. 51 (2013) 5–9.
[13] I.I. Bashter, Calculation of radiation attenuation coefficients for shielding concretes, Ann. Nucl. Energy. 24 (1997) 1389–1401, https://doi.org/10.1016/S0306-4549(97)00003-0.
[14] M.F. Kaplan, Concrete radiation shielding (1989).
[15] M.A. Çakıroğlu, Investigation of radiation shielding properties of polypropylene fiber reinforced shotcrete, Acta Phys. Pol. A. 129 (2016) 705–706.
[16] C. Thomas, J. Rico, P. Tamayo, J. Setién, F. Ballester, J.A. Polanco, J. Setién, J. A. Polanco, Neutron shielding concrete incorporating B4C and PVA fibers exposed to high temperatures, J. Build. Eng. 26 (2019), 100859.
[17] Y. Yarar, A. Bayülken, Investigation of neutron shielding efficiency and radioactivity of concrete shields containing colemanite, J. Nucl. Mater. 212 (1994) 1720–1723.
[18] D. Sarıyer, R. Küçer, N. Küçer, Neutron shielding properties of concretes containing boron carbide and ferro–boron, Procedia-Social, Behav. Sci. 195 (2015) 1752–1756.
[19] D.E. Volkman, Concrete for Radiation Shielding, in: Significance Tests Prop. Concr. Concr. Mater., ASTM International, 2006.
[20] P.K. Mehta, P.J.M. Monteiro, CONCRETE Microstructure, Properties and Materials (2017).
[21] T. Yasin, M.N. Khan, High density polyethylene/boron carbide composites for neutron shielding, E-Polymers. 8 (2008).
[22] M.A. Rafiee, T.N. Narayanan, D.P. Hashim, N. Sakhavand, R. Shahsavari, R. Vajtai, P.M. Ajayan, Hexagonal boron nitride and graphite oxide reinforced multifunctional porous cement composites, Adv. Funct. Mater. 23 (2013) 5624–5630.
[23] I. Akkurt, H.O. Tekin, A. Mesbahi, Calculation of detection efficiency for the gamma detector using MCNPX, Acta Phys. Pol. A. 128 (2015) 332–334.
[24] S. Sharifi, R. Bagheri, S.P. Shirmardi, Comparison of shielding properties for ordinary, barite, serpentine and steel–magnetite concretes using MCNP-4C code and available experimental results, Ann. Nucl. Energy. 53 (2013) 529–534, https://doi.org/10.1016/j.anucene.2012.09.015.
[25] D.E. Peplow, Monte Carlo shielding analysis capabilities with MAVRIC, Nucl. Technol. 174 (2011) 289–313.
[26] Y. Gao, C.R. Hughes, C.R. Greulich, J.E. Tulenko, A. Enqvist, J.E. Baciak, Radiation dose rate distributions of spent fuel dry casks estimated with MAVRIC based on detailed geometry and continuous-energy models, Ann. Nucl. Energy. 117 (2018) 84–97.
[27] P. Tamayo, J. Pacheco, C. Thomas, J. de Brito, J. Rico, Mechanical and Durability Properties of Concrete with Coarse Recycled Aggregate Produced with Electric Arc Furnace Slag Concrete, Appl. Sci. 10 (2020) 216.
[28] I. Sosa, C. Thomas, J.A. Polanco, J. Setién, P. Tamayo, High Performance Self-Compacting Concrete with Electric Arc Furnace Slag Aggregate and Cupola Slag Powder, Appl. Sci. 10 (2020) 773.
[29] M. Maslehuddin, A.A. Naqvi, M. Ibrahim, Z. Kalakada, Radiation shielding properties of concrete with electric arc furnace slag aggregates and steel shots, Ann. Nucl. Energy. 53 (2013) 192–196, https://doi.org/10.1016/j.anucene.2012.09.006.
[30] A.G. Hassan, H. Elkady, A.S. Faried, M.A. Hassan, M.E. Allam, Evaluation of electric arc furnace slag high strength shielding concrete on exposure to gamma 662 KeV, Case Stud. Constr. Mater. 13 (2020), e00416.
[31] J.T. San-José, I. Vegas, I. Arribas, I. Marcos, The performance of steel-making slag concretes in the hardened state, Mater. Des. 60 (2014) 612–619, https://doi.org/10.1016/j.matdes.2014.04.030.
[32] M. Maslehuddin, A.M. Sharif, M. Shameem, M. Ibrahim, M.S. Barry, Comparison of properties of steel slag and crushed limestone aggregate concretes, Constr. Build. Mater. 17 (2003) 105–112.
[33] S.I. Abu-Eishah, A.S. El-Dieb, M.S. Bedir, Performance of concrete mixtures made with electric arc furnace (EAF) steel slag aggregate produced in the Arabian Gulf region, Constr. Build. Mater. 34 (2012) 249–256.
[34] A. Santamaría, E. Rojí, M. Skaf, I. Marcos, J.J. González, The use of steelmaking slags and fly ash in structural mortars, Constr. Build. Mater. 106 (2016) 364–373, https://doi.org/10.1016/j.conbuildmat.2015.12.121.
[35] J.J. Chang, W. Yeih, T.J. Chung, R. Huang, Properties of pervious concrete made with electric arc furnace slag and alkali-activated slag cement, Constr. Build. Mater. 109 (2016) 34–40, https://doi.org/10.1016/j.conbuildmat.2016.01.049.
[36] R. Ince, K.E. Alyamaç, Determination of fracture parameters of concrete based on water-cement ratio, (2008).
[37] M.H. Kharita, S. Yousef, M. AlNassar, The effect of the initial water to cement ratio on shielding properties of ordinary concrete, Prog. Nucl. Energy. 52 (2010) 491–493.
[38] R. Şahin, R. Polat, O. İçelli, C. Çelik, Determination of transmission factors of concretes with different water/cement ratio, curing condition, and dosage of cement and air entraining agent, Ann. Nucl. Energy. 38 (2011) 1505–1511.
[39] A. Yadollahi, E. Nazemi, A. Zolfaghari, A.M. Ajorloo, Optimization of thermal neutron shield concrete mixture using artificial neural network, Nucl. Eng. Des. 305 (2016) 146–155.
[40] British Standards Institution, Tests for mechanical and physical properties of aggregates - Part 3: Determination of loose bulk density and voids, 1998.
[41] EN 1097-6:2014, EN 1097-6 - Tests for mechanical and physical properties of aggregates - Part 6: Determination of particle density and water absorption, (2014).
[42] M. de Fomento, Spanish structural concrete standard (EHE-08) -, In Spanish (2008).
[43] M. de Fomento, CÓDIGO ESTRUCTURAL - Título 2, Estructuras de hormigón. (2019).
[44] 197-1:2011 UNE-EN, Cement. Part 1: Composition, specifications and conformity criteria for common cements, (2011).
[45] EN 12350-2: 2009, Testing fresh concrete - Part 2: Slump-test, (2009).
[46] EN 12350-7, Testing fresh concrete - Part 7: Air content - Pressure methods, (2020).
[47] EN-12390-7, Testing hardened concrete - Part 7: Density of hardened concrete, (2009).
[48] UNE. 83980:2014, Concrete durability. Test methods. Determination of the water absorption, density and accessible porosity for water in concrete., (2014).
[49] EN 12390-3: 2099/AC:2011, Testing hardened concrete - Part 3: Compressive strength of test specimens, (2011)..
[50] EN 12390-13: 2013, Testing hardened concrete - Part 13: Determination of secant modulus of elasticity in compression, (2014)..
[51] EN-12390-6, Testing hardened concrete - Part 6: Tensile splitting strength of test specimens, (2010).
[52] B.T. Price, C.C. Horton, K.T. Spinney, RADIATION SHIELDING in The International Series of Monographs on Nuclear Energy, (1957).
[53] M. Voytchev, M.P. Iñiguez, R. Méndez, A. Mañanes, L.R. Rodríguez, R. Barquero, Neutron detection with a silicon PIN photodiode and 6LiF converter, Nucl. Instruments Methods Phys. Res. Sect. A Accel. Spectrometers, Detect. Assoc. Equip. 512 (2003) 546–552.
[54] B.S. 8500-2, Concrete-Complementary British Standard to BS EN 206-1. Part 2: Specification for Constituent Materials and Concrete, (2002).
[55] E.-S.-A. Waly, M.A. Bourham, Comparative study of different concrete composition as gamma-ray shielding materials, Ann. Nucl. Energy. 85 (2015) 306–310.
[56] B. Pomaro, F. Gramegna, R. Cherubini, V. De Nadal, V. Salomoni, F. Faleschini, Gamma-ray shielding properties of heavyweight concrete with Electric Arc Furnace slag as aggregate: an experimental and numerical study, Constr. Build. Mater. 200 (2019) 188–197.
[57] A.T. Şensoy, H.S. Gökçe, Simulation and optimization of gamma-ray linear attenuation coefficients of barite concrete shields, Constr. Build. Mater. 253 (2020), 119218.
[58] K. Zalegowski, T. Piotrowski, A. Garbacz, G. Adamczewski, Relation between microstructure, technical properties and neutron radiation shielding efficiency of concrete, Constr. Build. Mater. 235 (2020), 117389.
[59] S.S. Obaid, D.K. Gaikwad, P.P. Pawar, Determination of gamma ray shielding parameters of rocks and concrete, Radiat. Phys. Chem. 144 (2018) 356–360.